Supplementary Information (SI) for ChemComm.
This journal is © The Royal Society of Chemistry 2025

Electronic Supplementary Material (ESI) for ChemComm.
This journal is © The Royal Society of Chemistry 2022

Heterostructure CuSe/MnSe$_2$ with Se Vacancies of Rapid Ion Kinetics for Low-temperature Sodium-ion Batteries

*Qinghua Deng †, Kai Yang †, Zhiqian Li, Xiaodong Geng, Zhangyu Wang, Quanli Liu, Jiahe Li, and Nan Zhu**

[a] School of Chemistry, Dalian University of Technology, No.2 Linggong Road, Ganjingzi District, Dalian City, Liaoning Province, China, 116024.

E-mail: nanzhu@dlut.edu.cn

1. Experimental Section

Synthesis of CuCO$_3$/MnCO$_3$ precursor: 4.0 mmol of $CuSO_4{\cdot}5H_2O$ and 2.0 mmol $MnSO_4{\cdot}H_2O$ were put in 100 ml deionized water and stirred for a few minutes. Then, 10 ml alcohol was put in the above solution, and stirred until obtaining solution A. 28 mmol Na_2CO_3 was added into 100 ml deionized water and stirred for several minutes to prepare solution B. Under stirring, solution B was slowly added to solution A and stirred for 1.5 h. Then, this mixed solution was placed at room temperature until deposition appeared at the bottom of the beaker. The $CuCO_3$/$MnCO_3$ was gathered by washing three times with water and alcohol sequentially. After cooling at 60°C, $CuCO_3$/$MnCO_3$ precursor powder can be obtained.

Synthesis of CuSe/MnSe$_2$: 4 mmol of Se powder was dissolved in 5 ml hydrazine hydrate to form solution C. 241 mg of $CuCO_3$/$MnCO_3$ precursor was put in 20 ml deionized water to form solution D. Solution D was slowly added into solution C and stirred for 0.5 h. Then the CuSe/$MnSe_2$was synthesized by hydrothermal reaction at 180 °C for 12h. Finally, it was washed three times with water and ethyl alcohol sequentially.

Synthesis of Na$_3$V$_2$(PO$_4$)$_3$. The $Na_3V_2(PO_4)_3$ was prepared according to the previous literature with some modifications to a typical procedure. In a typical procedure, CH_3COONa, NH_4VO_3, $NH_4H_2PO_4$, and $C_6H_8O_7{\cdot}H_2O$ with a mass ratio of (3:2:3:1) were added into 50 mL deionized water for stirring 1 h to obtain a homogenous solution. The solvent was almost completely evaporated after the oil bath at 80 °C for 12 h. The as-obtained product was annealed at 350 °C for 5 h with a heating rate of 5 °C min^{-1} firstly and then annealed at 800 °C for 12 h with a heating rate of 5 °C min^{-1} under Ar/H_2 (95:5 v/v) atmosphere.

Characterization. The composition and crystal structure of as-prepared materials were determined by X-ray diffractometer (XRD, Bruker D8 Advanced, Germany), using monochromatic Cu Kα as a radiation source. The microstructure and morphology images were obtained using field emission scanning electron microscopy (NOVA Nano FESEM 450 FEI, US). The high-resolution transmission electron microscopy (HRTEM) was applied to test the heterostructure and selected-area electron diffraction (SAED). The X-ray photoelectron spectroscopy (XPS, ESCALAB 250Xi) experiments were performed using the surface analysis system of Al Kα (hv=1486.6 eV) to determine the elemental valence and bonding of the materials.

Electrochemical measurements. The electrochemical performance was evaluated by assembling CR2032 coin-cells. The active materials, ketjen black and polyvinylidene fluoride (7:2:1 by mass) were dispersed in N-methyl pyrrolidone (NMP) solvent to obtain a slurry. Then as-prepared slurry was respectively coated onto Cu foils and dried at 110 °C for 12 h in a vacuum oven. Typically, the loading mass of electrode was 1.0 mg cm^{-2}. The half-battery was assembly in Ar-filled glove box (O_2, H_2O < 0.01 ppm) with sodium metal as counter electrode, glass fiber as separator (GF/D, Whatman), and 1 M sodium trifluoromethane sulfonate ($NaSO_3CF_3$) was dissolved in diethylene glycol dimethyl ether (DGE) as electrolyte. For full cells, the cathode material is $Na_3V_2(PO_4)_3$@C (NVP@C). CuSe/$MnSe_2$ || NVP@C full cell was assembled in Ar-filled glove box (O_2, H_2O < 0.01 ppm), while the separator and electrolyte are the same as half-battery assembly. Galvanostatic discharge/charge (GCD) profiles and Galvanostatic intermittent titration technique (GITT) curves were obtained at room temperature on battery cycles (LAND CT-3001A, China). Cyclic voltammetry (CV) and electrochemical impedance spectroscopy (EIS) measurements were implemented on a CHI electrochemical workstation (660E). In situ impedance was tested using a AUTOLAB workstation (PSGTAT302, Autolab).

2. Results and discussion

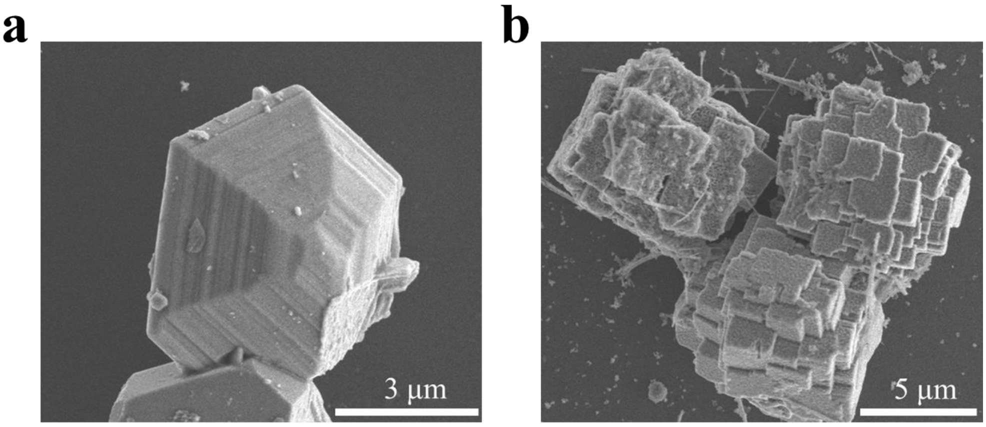

Fig. S1. (a) SEM image of pure CuSe, (b) SEM image of pureMnSe$_2$.

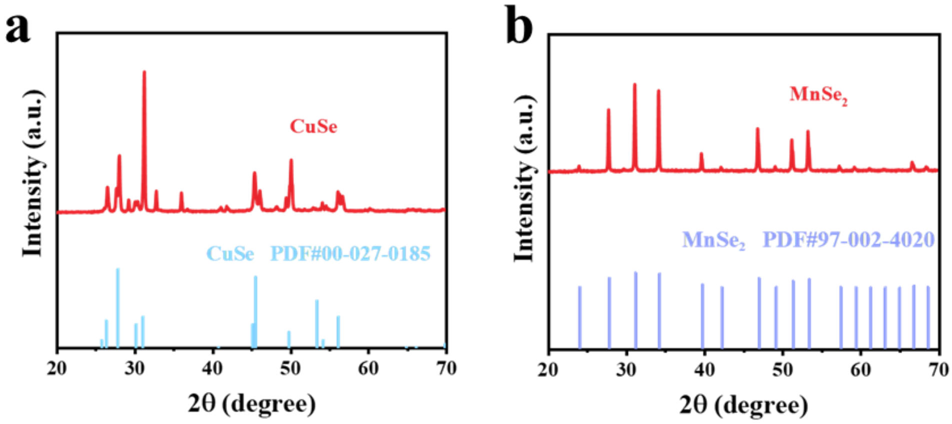

Fig. S2. XRD spectra of CuSe and MnSe$_2$ (a) XRD pattern of CuSe, (b) XRD pattern of MnSe$_2$.

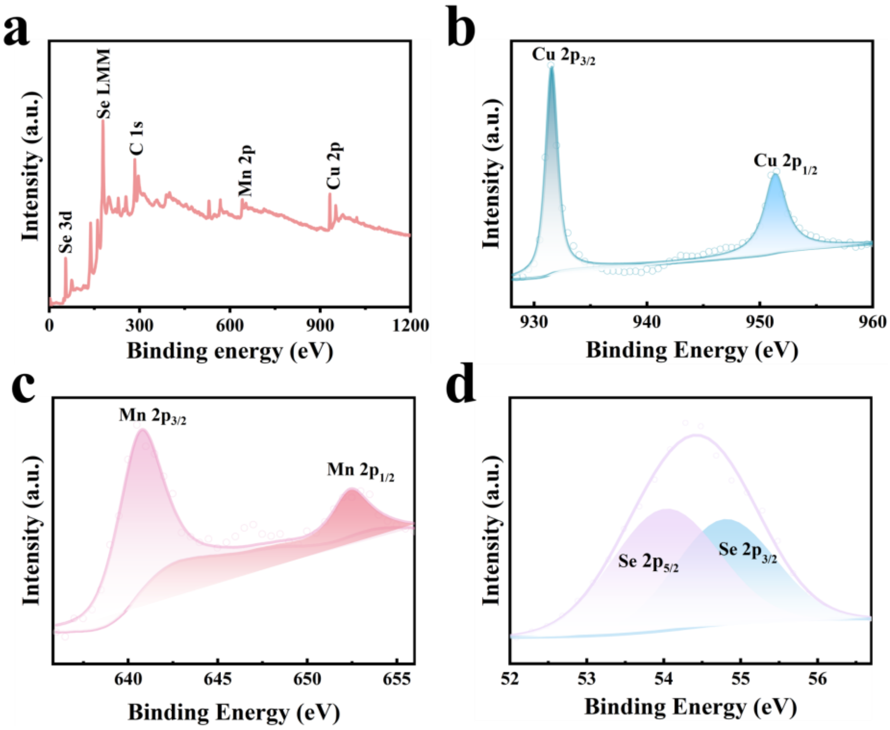

Fig. S3. XPS spectra of CuSe/MnSe$_2$. (a) XPS survey spectra of CuSe/MnSe$_2$; (b-d) High-resolution XPS spectra of Cu 2p, Mn 3d and Se 3d, respectively;

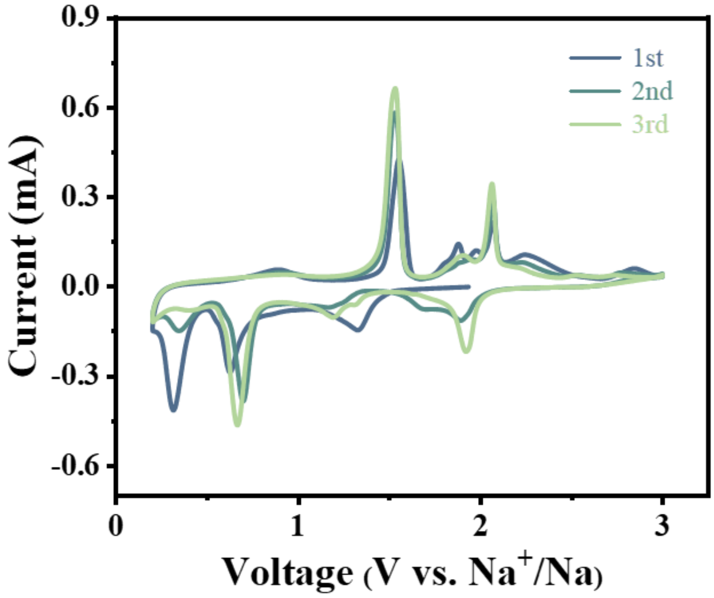

Fig. S4. CV curves of CuSe/$MnSe_2$.

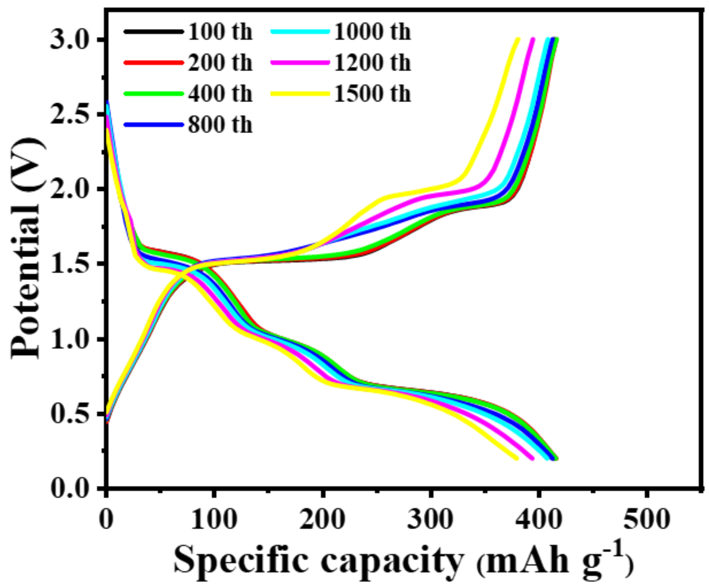

Fig. S5. GCD curves of $CuSe/MnSe_2$ at different cycles.

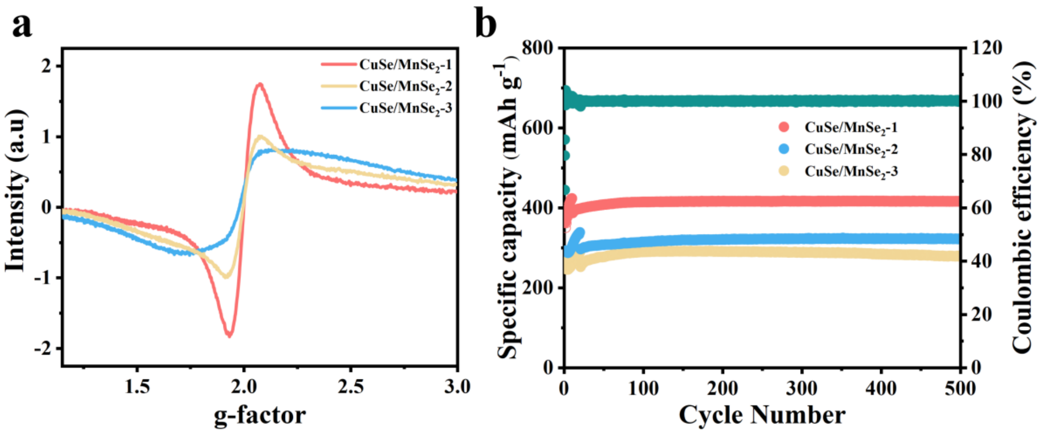

Fig. S6. (a) EPR diagram of three samples with different Se vacancies. (b) Cycle performance of CuSe/MnSe2 at 3.0 A g-1 of three samples with different Se vacancies.

There prepares three samples with different Se vacancies. They are prepared following the method described in the supporting information. The only difference between them lies in the amount of hydrazine hydrate used during selenization: 5 ml for CuSe/MnSe$_2$-1, 3 ml for CuSe/MnSe$_2$-2 and 7 ml for CuSe/MnSe$_2$-3.

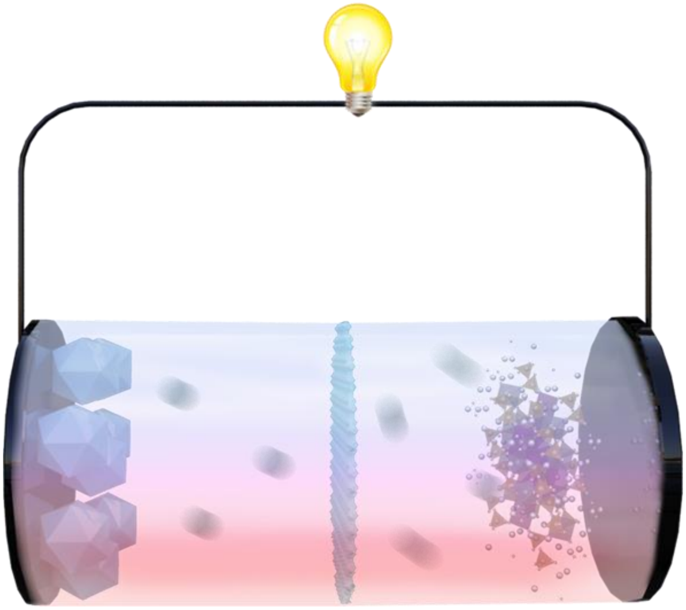

Fig. S7. Schematic of $CuSe/MnSe_2$ || NVP@C full cell.

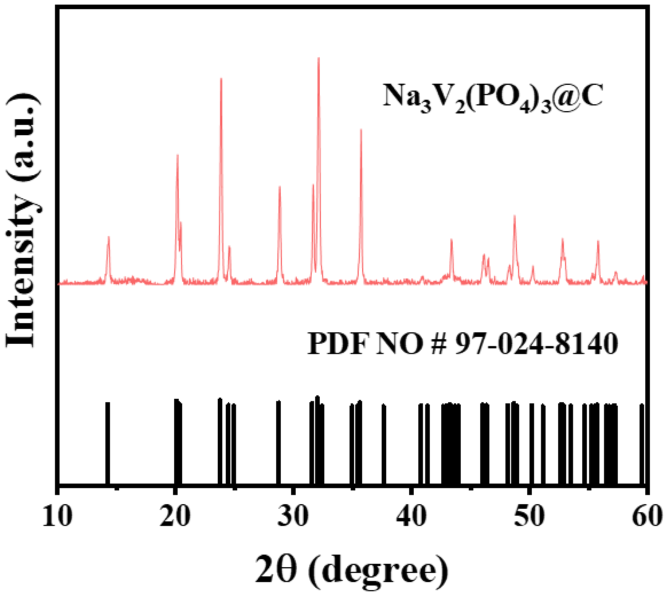

Fig. S8. XRD pattern of $Na_3V_2(PO_4)_3$@C.

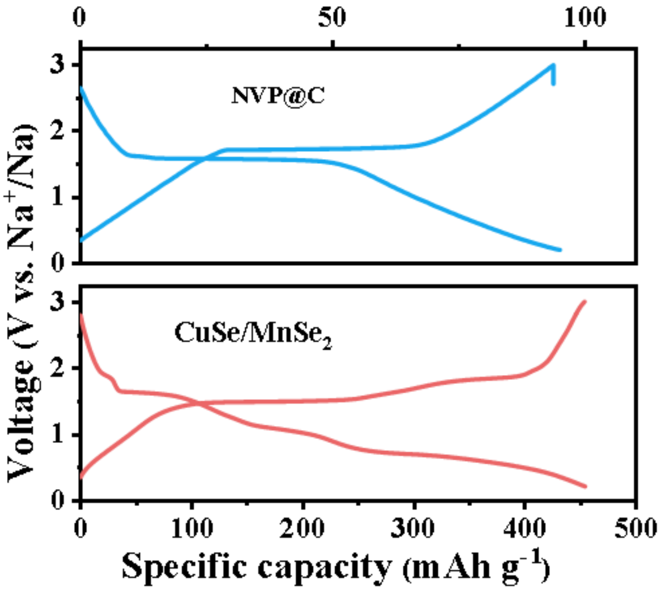

Fig. S9. Galvanostatic charge-discharge curve of $Na_3V_2(PO_4)_3$@C cathode and CuSe/$MnSe_2$ anode.

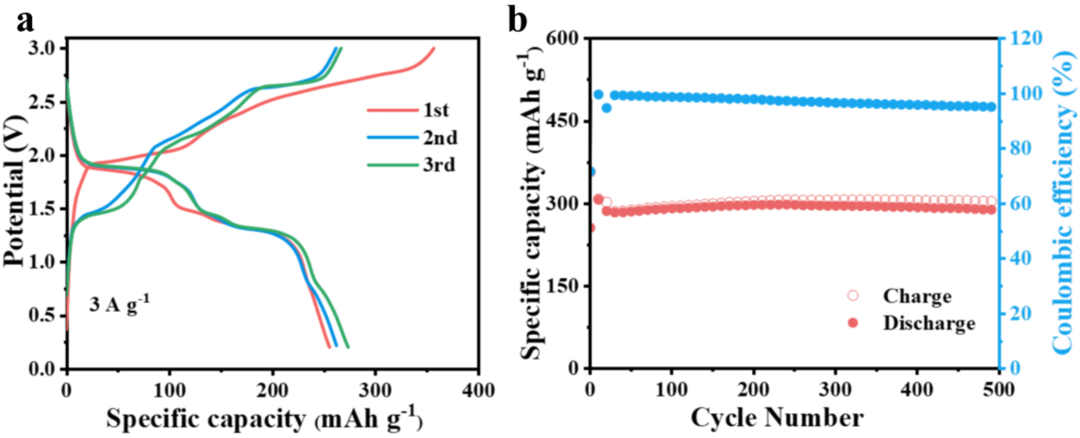

Fig. S10. (a) Galvanostatic charge-discharge curve of full cell. (b) Cycle stability of full cell at 3 A g^{-1}.

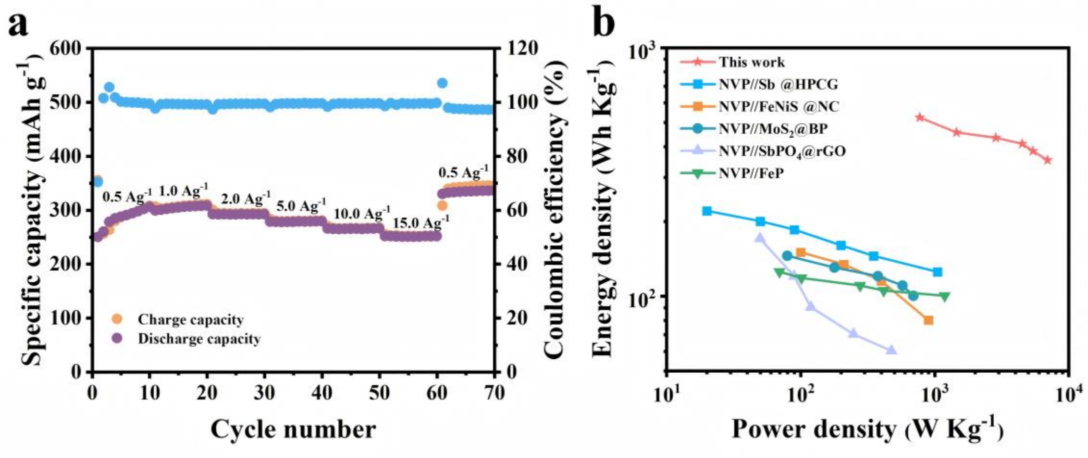

Fig. S11. (a) CuSe/MnSe2 || NVP@C full cell rate performance diagram. (b) Comparison of the energy/power density of the CuSe/MnSe2 || NVP@C device with previously reported SIBs full battery[3-7].

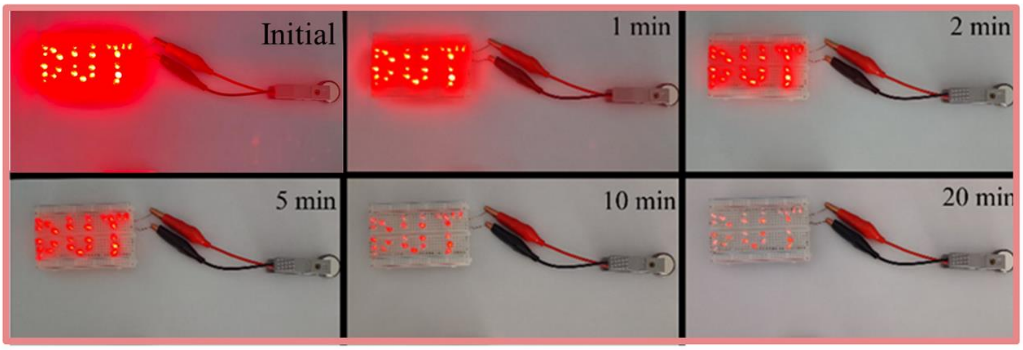

Fig. S12. The application of LEDs lit by full cell during 0-20 minutes.

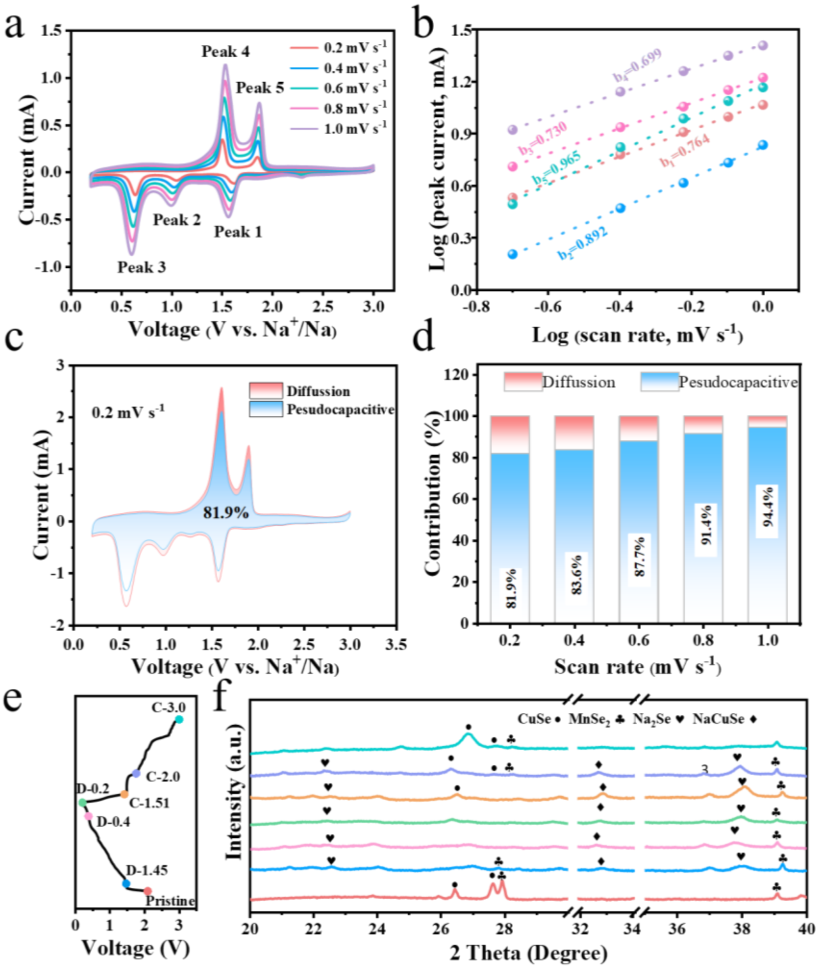

Fig. S13. Evaluation of electrochemical kinetic behavior for CuSe/MnSe$_2$. (a) CV curves of CuSe/MnSe$_2$ at various scan rates from 0.2 to 1.0 mV s^{-1}; (b) Determination of b value based on the relationship between peak current and scan rate; (c) CV patterns with capacitive contribution at 0.2 mV s^{-1}; (d) Proportions of capacitive contribution at various rates; (e) First charge-discharge curve; (f) Ex-situ XRD of CuSe/MnSe$_2$ during sodiation/desodiation process.

To investigate the mechanism of specific capacity/cycle performance of CuSe/MnSe$_2$ in SIBs, reaction dynamics analysis during Na$^+$ diffusion is explored by CV curves. Charge storage consists of ion diffusion control contribution and pseudo-capacitance control contribution. The capacity contribution can be determined by power law formula of peak current (i) and scan rate (v), Relationships are as follows

$$i = a\nu^{b} \tag{1}$$

$$\log i = b \log v + \log a \tag{2}$$

Where i and *v* are variable quantities, and a and b are constants. When b value approaches to 0.5, charge storage mechanism is dominated by ion diffusion control. When approaching to 1.0, capacitance control process dominates.

CV curves present an identical shape with five major peaks (Figure 4a), indicating remarkable reversibility of CuSe/MnSe$_2$. The calculated b-values are 0.764, 0.892, 0.730, 0.699, and 0.965, respectively (Figure 4b), indicating that capacitive-controlled process is dominant and accompanied with diffusion-controlled process.

Furthermore, capacitive contribution at different scan rates is calculated by Equation:

$$i = k_1 v + k_2 v^{0.5} \tag{3}$$

The calculated capacitive contribution ratios are determined to be 81.9%, 83.6%, 87.7%, 91.4%, and 94.4% at scan rates of 0.2, 0.4, 0.6, 0.8, and 1.0 mV s^{-1} respectively (Figure 4c), indicating gradual increase in capacitive contribution (Figure 4d). High pseudo-capacitive contribution can be attributed to effective exposure of active sites, excellent interfacial properties, and accelerated ion diffusion rate endowed by high-quality heterostructure and Se vacancies. There provides additional shuttle paths for sodium ions and promotes the kinetics of electrochemical reaction.

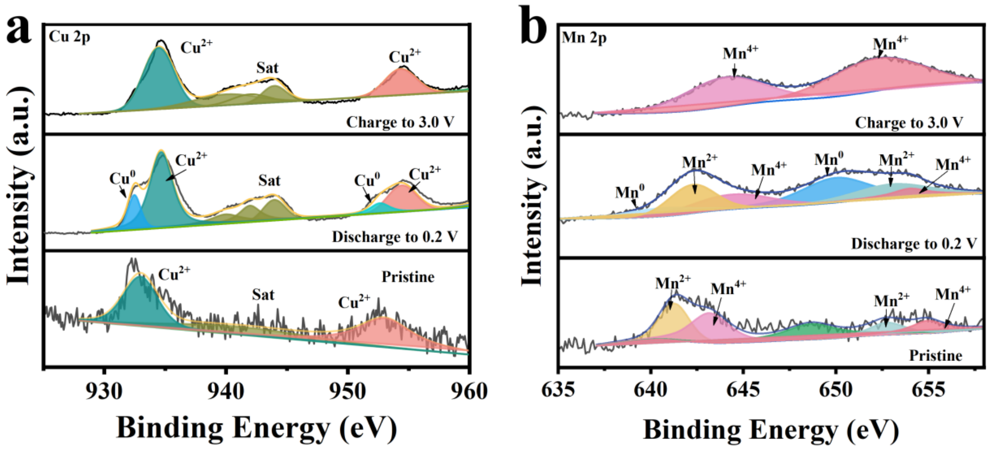

Fig. S14. (a) Cu 2p at different voltage states for the CuSe/MnSe$_2$, (b) Mn 2p at different voltage states for the CuSe/MnSe$_2$.

At the fully discharged state (0.2 V), the characteristic peaks at 932.5 and 952.4 eV in the Cu 2p spectra, corresponding to the Cu^0 electronic state, clearly confirmed the complete reduction of CuSe to metallic Cu. Upon charging to 3.0 V, the Cu^0 peaks vanished, and the peak positions reverted to those of Cu^{2+} in the initial CuSe phase, demonstrating the reversible transformation of the CuSe. Analysis of the Mn 2p spectra further validated this mechanism: the dual peaks at 639.2 and 650.2 eV observed at 0.2 V discharge indicated the reduction of MnSe$_2$ to metallic Mn^0, while a single Mn^{4+} peak emerged after charging to 3.0 V, signifying the regeneration of the MnSe$_2$ lattice. These findings align well with the recovery of the main diffraction peaks in the ex situ XRD patterns of CuSe/MnSe$_2$.

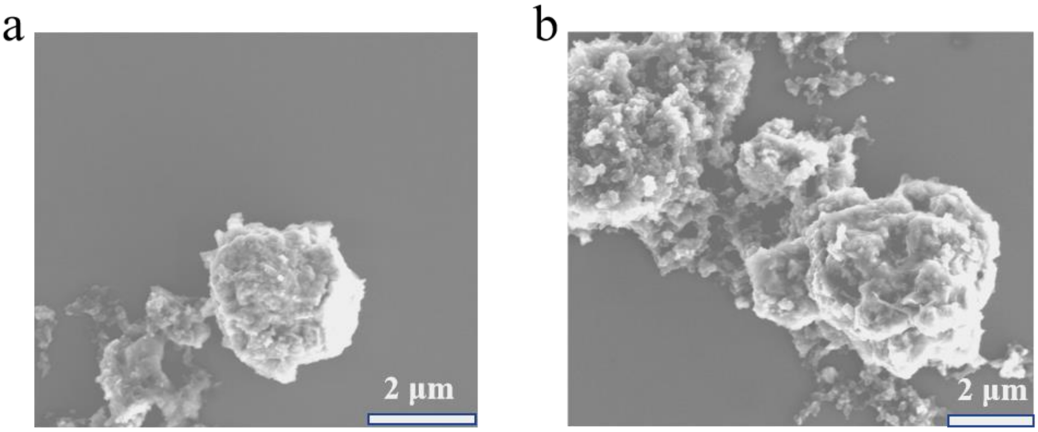

Fig. S15. (a) SEM image of CuSe/MnSe$_2$ after 500 cycle, (b) SEM image of CuSe/MnSe$_2$ after 1500 cycle.

Table S1. The rietveld refinement results for CuSe/$MnSe_2$.

Phase composition		CuSe	$MnSe_2$
Contents		91.32	8.68
Space group		P63/mmc	Pa-3
Cell paracmeters	A(Å)	3.97650	6.43665
	b(Å)	3.97650	6.43665
	c(Å)	17.25317	6.43665
	α(°)	90.00000	90.00000
	β(°)	90.00000	90.00000
	γ(°)	120.00000	90.00000
	Volume(Å3)	236.267	266.673

Table S2. Atoms information of CuSe according to the XRD rietveld results.

Name	x	y	z	occ.socc.	Mult
Cu1	0.3333	0.6667	0.75	0.083	2
Cu2	0.3333	0.6667	0.11626	0.167	4
Se1	0.3333	0.6667	0.25	0.083	2
Se2	0	0	0.0584	0.167	4

Table S3. Atoms information of $MnSe_2$ according to the XRD rietveld results.

Name	x	y	z	occ.socc..	Mult
Mn1	0.00000	0.00000	0.00000	0.167	4
Se1	0.39419	0.39419	0.39419	0.333	8

Table S4. Experimental reagents

Chemical reaction	Manufacturer	Purity
$N_2H_4 \cdot H_2O$	Sinopharm Chemical Reagent Co, Ltd	AR
NH_4HCO_3	Sinopharm Chemical Reagent Co, Ltd	AR
Se	Sinopharm Chemical Reagent Co, Ltd	AR
C_2H_5OH	Sinopharm Chemical Reagent Co, Ltd	AR
$CuSO_4 \cdot 5H_2O$	Sinopharm Chemical Reagent Co, Ltd	AR
$MnSO_4 \cdot H_2O$	Sinopharm Chemical Reagent Co, Ltd	AR
CH_3COONa	Tianjin Damao Chemical Reagent Factory	AR
NH_4VO_3	Tianjin Damao Chemical Reagent Factory	AR
$NH_4H_2PO_4$	Tianjin Damao Chemical Reagent Factory	AR
$C_6H_8O_7 \cdot H_2O$	Sinopharm Chemical Reagent Co, Ltd	AR
NH_4VO_3	Sinopharm Chemical Reagent Co, Ltd	AR

Table S5 Performance summary of Materials for SIBs anode(DC: discharge capacity,CD: current density, RC: reversible capacity, CN: cycle number).

Materials	1st[DC/CD]	Cycle data [RC/CN/CD]	Rate capability [RC/CD]	Reference
This work	567.8/0.2	380.3/1500/3	323.1/15	
$FeSe_2$-xS_x	458.1/0.2	374/2000/10	306/50	14
Sb@$InSbS_3$@rGO	719/0.1	211/1200/2	210/6.4	15
NLM	100.1/0.2	97.3/150/0.2	82.7/10	16
MSC	379.5/0.2	357/1000/10	309.4/10	17
3DOHP ZnSe@N, C	421.4/0.1	233.1/800/10	179.9/10	18
ZnSe@C@rGO	503.1/0.1	223.7/1000/5	141.7/10	19
ZnSe/MWCNT	458.6/0.1	281.7/300/4	279.4/10	20
$NiSe_2$	535/0.1	318/800/1	310/10	21
$CoSe_2$/O-C	373.7/0.5	346/3500/15	274/5	22

3. Reference

1. Y. Hu, C. Fu,and S. Chai, Adv. Powder Mater., 2023, 2, 100093.
2. G. Liu, X. Yin and J. Xie, Inorg. Chem. Front., 2025, 12, 647 – 657.
3. S. Shi, C. Sun, X. Yin, Adv. Funct. Mater., 2020, 30, 1909283.
4. Y. Wang, Q. Wang, J. Wu, Alloys Compd., 2022, 914, 165336.
5. J. Pan, S. Chen, Q. Fu, ACS Nano, 2018, 12, 12869 – 12878.
6. C. Zhang, T. Liang, H. Dong, Mater. Chem. Front., 2021, 5, 6639 – 6647.
7. H. Chen, P. Tian, L. Fu, Chem. Eng. J., 2022, 430, 132688.
8. K. Xie, X. Liu, K. Xia, Energy Chem., 2024, 97, 747-756.
9. Y. Li, J. Zhang, Q. Chen, Adv. Mater., 2021, 33, 2100855.
10. X. Wang, Y. Xu, X. Liu ,. Energy Chem., 2024, 95, 336-347.
11. I. Hussain, S. Sahoo, C. Lamiel, Energy Storage Mater., 2022, 47, 13-43.
12. Y. Wan, B. Huang, W. Liu et al., Adv. Mater., 2024, 36, 2404574.
13. M. Li, H. Zhuo, Q. Jing, Carbon Energy, 2024, 6, e546.
14. S. Xiao, J. Jiang, Y. Zhu, Adv. Powder Mater., 2023, 2, 100120.
15. J. Y. Ren, X. L. Yu, C. M. Chen, Rare Met., 2024, 43, 2080 – 2092.
16. L. Gan, X. G. Yuan, J. J. Han, Carbon Neutralization, 2023, 2, 10.
17. H. Zhang, B. Liu, Z. Lu, Small, 2023, 19, 2207214.
18. X. Li, Z. Han, W. Yang, Adv. Funct. Mater., 2021, 31, 2106194.
19. S. Men, H. Zheng, D. Ma, J. Energy Chem., 2021, 54, 124.
20. Y. Zhou, X. Sun, A. Fan, Appl. Surf. Sci., 2021, 538, 148194.
21. L. Yu, L. Shao, S. Wang, Mater. Today Phys., 2022, 22, 100593.
22. W. Sun, W. Zhao, S. Yuan, Adv. Funct. Mater., 2021, 31, 2100156.
23.
24. Q. Zhu, A. Xu, H. Chen, C. Liu, Y. Yan and S. Wu, ACS Appl. Mater. Interfaces, 2023, 15, 12976 – 12985.
25. K. Xie, X. Liu, K. Xia, Energy Chem., 2024, 97, 747-756.
26. Y. Li, J. Zhang, Q. Chen, Adv. Mater., 2021, 33, 2100855.
27. X. Wang, Y. Xu, X. Liu ,. Energy Chem., 2024, 95, 336-347.
28. I. Hussain, S. Sahoo, C. Lamiel, Energy Storage Mater., 2022, 47, 13-43.
29. Y. Wan, B. Huang, W. Liu et al., Adv. Mater., 2024, 36, 2404574.
30. M. Li, H. Zhuo, Q. Jing, Carbon Energy, 2024, 6, e546.
31. X. Ma, Y. Li, X. Long, H.-C. Luo, C. Xu, G. Wang and W. Zhao, J. Energy Chem., 2023, 77, 227 – 238.
32. K. Qian, L. Li, D. Yang, B. Wang, H. Wang, G. Yuan, J. Bai, S. Ma and G. Wang, Adv. Funct. Mater., 2023, 33, 2212070.
33. L. Shao, S. Wang, J. Qi, Z. Sun, X. Shi, Y. Shi and X. Lu, Mater. Today Phys., 2021, 19, 100422.
34. J. Xia, Y. Yuan, H. Yan, J. Liu, Y. Zhang, L. Liu, S. Zhang, W. Li, X. Yang and H. Shu, J. Power Sources, 2020, 449, 227559.
35. C. Xu, Y. Yang, K. Chen, G. Ma, Y. Wang, Z. Li, Z. Zhou, Z. Wu, S. Che, C. Ding, Chem. Eng. J., 2024, 497, 154875.
36. H. Zheng, J. Wang, H. Li, S. Deng, Y. Zuo, W. Yan and J. Zhang, J. Mater. Chem. A, 2022, 10, 16268 – 16279.